

Advances in solution-processed near-infrared light-emitting diodes

Maria Vasilopoulou^{1,1,*}, Azhar Fakharuddin^{2,1}, F. Pelayo García de Arquer^{3,4}, Dimitra G. Georgiadou^{5,6}, Hobeom Kim⁷, Abd. Rashid bin Mohd Yusoff⁸, Feng Gao⁹, Mohammad Khaja Nazeeruddin⁷, Henk J. Bolink^{10,*}, Edward H. Sargent^{3,*}

¹Institute of Nanoscience and Nanotechnology, National Center for Scientific Research Demokritos, 15341 Agia Paraskevi, Attica, Greece

²Department of Physics, University of Konstanz, 78464 Konstanz, Germany

³Department of Electrical and Computer Engineering, University of Toronto, Toronto, ON, M5S 3G4, Canada

⁴ICFO - Institut de Ciències Fotòniques, The Barcelona Institute of Science and Technology, Barcelona 08860, Spain

⁴Zepler Institute for Photonics and Nanoelectronics, University of Southampton, SO17 1BJ Southampton, United Kingdom

⁵Department of Physics, Imperial College London, SW7 2AZ London, United Kingdom

⁶Institute of Chemical Sciences and Engineering, École Polytechnique Fédérale de Lausanne (EPFL), Rue de l'Industrie 17, CH-1951 Sion, Switzerland

⁷Department of Chemical Engineering, Pohang University of Science and Technology (POSTECH), Pohang, Gyeongbuk 37673, Republic of Korea

⁸Department of Physics, Chemistry and Biology (IFM), Linköping University, Sweden

⁹Instituto de Ciencia Molecular, Universidad de Valencia, Calle Catedrático Jose Beltrán 2, 46980 Paterna, Spain

24 [†]These authors contributed equally to this work. *Email: m.vasilopoulou@inn.demokritos.gr,
25 henk.bolink@uv.es, ted.sargent@utoronto.ca

26

27 **Abstract**

28 **Near-infrared light-emitting diodes based on solution-processed semiconductors, such as organics,**
29 **halide perovskites and colloidal quantum dots, have emerged as a viable technological platform**
30 **for biomedical applications, night vision, surveillance and optical communications. The recently**
31 **gained increased understanding of the materials structure-photophysical property relationship**
32 **has enabled the design of efficient emitters leading to devices with external quantum efficiencies**
33 **exceeding 20%. Despite significant strides made, challenges remain in achieving high radiance,**
34 **reducing efficiency roll-off, and extending operating lifetime. This review summarizes recent**
35 **advances on emissive materials synthetic methods and device key attributes that collectively**
36 **contribute to improved performance of the fabricated light-emitting devices.**

37

38 Light-emitting diodes (LEDs) with emission in the near-infrared (NIR) part of the spectrum (700-2500
39 nm) (termed as NIR-LEDs) support a large variety of applications such as optical diagnosis and
40 biomedical imaging¹, optical communication, remote sensing, security, night vision and data storage².
41 The specific application field determines the spectral range of interest within the NIR (Fig. 1a). With
42 regard to *in vivo* bioimaging, the semi-transparency of biological tissues, oxygenated and deoxygenated
43 blood in specific NIR wavelength regions, also known as biological windows, makes NIR particularly
44 appealing for optical imaging, biomedical sensing and photodynamic therapy. In the field of optical
45 wireless communications, the spectral range is also divided in bands, which correlate with the
46 wavelength regions where optical fibres have small transmission losses³. NIR-LEDs are also in demand

47 for security authentication, optogenetics, life-cycle management of crops, light fidelity and
48 surveillance⁴.

49 Common NIR-LEDs are epitaxial heterostructures of III-V inorganic semiconductors (e.g. GaAs,
50 InGaAs, InGaAlAs)⁵⁻⁷. Commercially available products also employ inorganic phosphors, namely
51 compounds doped with transition metals⁸, or rare-earth trivalent ions⁹. An external quantum efficiency
52 (EQE) of 72% at 880 nm has been reported for an AlGaAs/GaAs/AlGaAs III-V-LED⁶, and 44.5% at 775
53 nm for LEDs based on LaMgGa₁₁O₁₉:Cr³⁺ phosphors¹⁰. However, III-V LEDs require post fabrication
54 substrate replacement with high reflective mirror structures to increase their poor power output
55 originating from the refractive index mismatch between those materials (>3.0)⁷ and common substrates.
56 Additionally, inorganic phosphors require very high temperature sintering treatment (above 1000 °C).
57 These processing requirements are an obstacle for low-cost, handheld portable implementations.

58 Organic (OSCs)¹¹, metal-halide perovskite (HPs)¹², and colloidal quantum dot (QD)¹³
59 semiconductors, can be processed using low cost and low temperature methods on a wide variety of
60 substrates. For example via solution-based processes such as ink-jet printing, doctor blade and spray
61 coating (Fig. 1b). These qualities make these thin-film LEDs a potentially cost-efficient alternative to
62 their inorganic counterparts and of interest for emerging applications in wearable, implantable and
63 portable electronics. Although there has been progress in different performance metrics such as EQE,
64 challenges remain in reducing the efficiency roll-off, increasing lifetime and to alleviate toxicity issues
65 of some of the emissive materials. In this review, we provide an overview of strategies used to achieve
66 high performance in these thin-film LEDs. The material and device design considerations affecting the
67 peak emission wavelength, efficiency and operational stability are described. We conclude with an
68 outlook on future improvements linked to specific applications.

69

70 **Toward high-efficiency solution-processed NIR-LEDs**

71 The key performance metrics of a NIR-LED are the EQE, optical output power (P) and radiance (R)
72 (Box 1). The EQE is the product of four parameters namely the probability of electrons and holes
73 recombining (γ), the probability of radiative recombination to occur (r), the photoluminescence quantum
74 yield (PLQY or ϕ_{PL}) of the emitter and the light outcoupling efficiency (η_{out}) that describes the
75 probability a photon escapes the device in the viewing direction. The parameters r and ϕ_{PL} are intrinsic
76 properties of the selected emitters, γ also depends on the device configuration and the charge injection
77 interlayers whereas η_{out} depends on the refractive indices of the functional layers and the substrate. To
78 maximize the EQE, it is crucial to simultaneously optimize all four parameters¹⁴⁻¹⁶. In the following
79 sections, we present the recent progress on the development of narrow bandgap OSC, HP and QD
80 emitters and devices with efficient and stable electroluminescence in the NIR.

81

82 **Recent progress in NIR organic light-emitting diodes**

83 To maximize organic light-emitting diode (OLED) efficiency, both r and ϕ_{PL} should approach unity; the
84 latter is defined as the ratio of the radiative (k_r) to total decay rates ($k_r + k_{nr}$). Spin statistics suggest that
85 r is upmost 25% for pure fluorescent emitters and nearly 100% for phosphorescent¹⁷, and thermally
86 activated delayed fluorescent (TADF)¹⁸ ones. Furthermore, *via* triplet-triplet annihilation (TTA), r can
87 reach $25\% + 0.5 \times 75\% = 62.5\%$ ¹⁹, under the requirement that the singlet populated states are spin-
88 allowed. Finally, singlet-fission in the presence of a suitable sensitizer can potentially increase r up to
89 200% ²⁰ (Fig. 2a-c).

90 To extend the emission of π -conjugated molecules to the NIR, the gap between the highest occupied
91 molecular orbital (HOMO) and lowest unoccupied molecular orbital (LUMO) must be reduced²¹. This
92 can be accomplished by a number of chemical modifications that extend the effective conjugation length

93 or selectively influence the energy level of the HOMO or the LUMO (Fig. 2d)²². The introduction of
94 electron-withdrawing (acceptor) substituents in the aromatic ring can reduce its aromatic character and
95 as a result reduce the electron confinement. Inserting electron-releasing (donor) substituents to a π -
96 conjugated molecule tends to increase the HOMO energy more than that of the LUMO, and as such
97 effectively reducing the gap between them. Another approach relies on the planarization and
98 rigidification of the conjugated system.

99 However, there is an intrinsic quenching mechanism known as the “energy gap law” according to
100 which, as the energy gap decreases, coupling of the zero-vibration level of the lowest excited state
101 (either singlet, S_1 , or triplet, T_1) with the higher vibration levels of the ground state (S_0) promotes non-
102 radiative recombination pathways²³. The energy gap law induces fundamental constraints on how much
103 the energy gap of OSCs can be effectively decreased, thus limiting the emission of many OSC emitters
104 below 900 nm (Fig. 2e).

105 Most fluorescent molecules have two electrons in their HOMOs at the ground state, referred to as “a
106 closed shell”. Upon excitation, the excited state is either a singlet or triplet. Most organic molecules can
107 only harvest the singlet-excited states radiatively at room temperature, as the transition from a triplet to
108 the ground state is forbidden. This means that these molecules are subjected to $r \sim 25\%$. As the result,
109 NIR-OLEDs using conventional closed-shell emitters, without assistant’s sensitization and in the
110 absence of outcoupling structures or photon recycling, are limited to EQEs of 5%^{24,25}.

111 Open-shell radical emitters, have a singly occupied molecular orbital (SOMO) in the ground state,
112 giving an overall spin-1/2 doublet (D_0). If holes and electrons are injected into the HOMO and SOMO,
113 respectively, a fluorescence doublet excited state (D_1) is obtained which gives a spin-allowed emission
114 and r approaches unity (Fig. 2f)²⁶⁻²⁸. One such organic radical, termed as TTM-3NCz, incorporating 3-
115 substituted-9-(naphthalen-2-yl)-9H-carbazole (3NCz) and 3-substituted-9-phenyl-9H-carbazole (3PCz)

116 added to the tris(2,4,6-trichlorophenyl)methyl (TTM) core, has recently achieved a high ϕ_{PL} of $(85.6 \pm$
117 $5.4) \%$ when doped in CBP²⁸. The fabricated OLEDs emitted at 710 nm with EQEs of 27 and 10% at
118 current densities (J) of 5×10^{-3} and 1 mA cm^{-2} , respectively.

119 In TADF emitter based LEDs excited long living triplet states can decay *via* the singlet states
120 through reverse intersystem crossing radiatively (Fig. 1a) and as a result, r can approach unity. To
121 enable this process it is essential that the singlet-triplet energy difference (ΔE_{ST}) is small. Generally,
122 ΔE_{ST} is minimized by localizing the HOMO and LUMO orbitals on different fragments of the emitting
123 molecule. This is observed in systems containing spatially separated donor (D) and acceptor (A)
124 heterocycles with twisted linkages. Emission from such molecules occurs from intramolecular charge
125 transfer (CT) states. It is therefore difficult to achieve a low energy gap, small ΔE_{ST} and a large
126 fluorescence rate (k_F) in one molecule²⁹. The first successful TADF NIR-OLED employed a
127 phenanthrene-based molecule with a small ΔE_{ST} of 0.13 eV as non-doped emitter; it achieved an EQE of
128 2.1% at a peak emission of 710 nm³⁰. Since then, several studies have also reported NIR
129 electroluminescence (EL) from TADF molecules, albeit with EQE values hardly exceeding 10%³¹⁻³⁴.
130 These devices were mostly based on multiple donor-acceptor (D_i-A_j) structures. One successful example
131 is an emitter composed of two triphenylamine donor and one acetylacetonate boron difluoride acceptor
132 (inset in Fig. 2g)³². This material exhibited a ϕ_{PL} up to 70% when doped ($\sim 6\%$) in a 4,4'-bis(N-
133 carbazolyl)-1,10-biphenyl (CBP) host (Fig. 2g). The LEDs showed a maximum EQE of 10.0% (at 721
134 nm) and a high radiance of $3000 \text{ W sr}^{-1} \text{ m}^{-2}$, albeit at a very high J , of 1000 mA cm^{-2} . Recently, NIR
135 TADF emitters employing simpler D-A structures having strong and planar acceptor units were found to
136 enable J -aggregate formation with strong intermolecular CT³⁵. Favored by the fast radiative decay rates
137 of the aggregated emitters, the fabricated OLEDs reached an EQE of 14.1% (at 700 nm and $J=10^{-2} \text{ mA}$
138 cm^{-2}). Through donor substitution, the intermolecular CT was further strengthened and tuned the OLED

139 emission at 1010 nm³⁶. Similarly, a D-A acenaphthene-based emitter greatly stabilized the
140 intramolecular CT; the fabricated OLEDs displayed a peak EL at 904 nm³⁷. Notably, apart from
141 leveraging NIR emission, TADF molecules were recently applied as assistant dopants in
142 hyperfluorescent OLEDs^{38,39}, demonstrating promising EQEs up to 3.8% ($J=5 \times 10^{-2}$ mA cm⁻²) with a
143 narrow EL peak (full-width at half-maximum, FWHM, of 40 nm) centered at 840 nm³⁸.

144 The most successful examples of NIR OSCs, are organometallic complexes based on third-row
145 transition metal elements, such as platinum (Pt(II)), osmium (Os(II)) and iridium (Ir(III)). In these
146 emitters $r = 1$ as all the triplet states can decay radiatively at room temperature due to presence of strong
147 spin-orbit coupling enabled by the metal element. So far, Pt(II) phosphors are the most efficient NIR
148 emitters due to the strong metal-metal-to-ligand charge transfer (MMLCT) transition character at the
149 excited state manifolds and the shortest radiative lifetime for phosphorescence⁴⁰. Os(II) phosphors
150 represent the next more efficient class of NIR emitters due to the high metal-to-ligand charge transfer
151 (MLCT) contribution, originating from the lower oxidation potential of the metal d_{π} orbitals combined
152 with reduced radiative lifetime to sub-microsecond region. In contrast, Ir(III) phosphors present longer
153 radiative lifetime and inferior efficiency compared to Pt(II) and Os(II) ones^{41,42}. For example, the state-
154 of-the-art Ir(III)-based NIR-OLEDs have reached a maximum EQE of 9.59% (at 706 nm) by using
155 cyano groups attached in a commercial red emitter (Ir(piq)₂(acac))⁴³. The record performing Os(II)-
156 based NIR-OLEDs employ a series of trans-substituted complexes combining pyrazinyl azolate chelates
157 and dimethyl(phenyl)phosphane ancillaries⁴⁴. They achieved a maximum EQE of 11.5% (at 710 nm),
158 which remained quite high (~8.2%) for a high $J=100$ mA cm⁻². A series of terdentate cyclometallated
159 Pt(II) complexes (PtL²Cl) of high planarity enabled NIR-OLEDs with a peak excimer emission at ~700
160 nm and EQE of 14.5%⁴⁵.

161 A breakthrough in NIR-OLEDs was accomplished through the strategic design of a series of 2-
162 pyrazinylpyrazolate Pt(II) fluorinated compounds (1-3) (Fig. 2h); they achieved extraordinary ϕ_{PL} of 81,
163 55 and 85% in thin films at peak emission of 740, 703 and 673 nm, respectively (Fig. 2i)⁴⁶. OLEDs
164 based on compound 1 exhibited a remarkable EQE of 24% (at 740 nm) originating from exciton-like
165 emission along the $5d_{z^2}$ direction of edge-on molecular *J*-aggregates. Owing to the short stacking
166 distance in these aggregates, a strong interaction among HOMO and LUMO levels was achieved, which
167 strongly prohibited non-radiative deactivation paths through exciton-optical phonon coupling according
168 to the energy gap law. More recently, the same group demonstrated that delocalized excitonic aggregates
169 can decouple the exciton band from highly vibrational ladders in the ground state, thus further enhancing
170 the ϕ_{PL} in the NIR region^{40,47}. On this basis, they successfully fabricated NIR-OLEDs achieving a high
171 EQE of 2.18% in the NIR region of 890-930 nm⁴⁰; added to the merits, these devices exhibited
172 negligible efficiency roll-off for *J* up to 500 mA cm⁻². In a recent work a non-doped EML consisting of
173 only the Pt(II) emitters enabled OLEDs with EQEs > 10 % at 794 nm (*J*=100 mA cm⁻²)⁴⁸, with low
174 efficiency roll-off. Compared with host-guest EML, the complexity is reduced when no host is used, yet
175 the required amount of Pt containing emitters is increased.

176 Pt-metalloporphyrins also enable NIR electroluminescence with narrow emission spectra. As an
177 example, OLEDs based on Pt(II)-tetraphenyltetrabenzoporphyrin (Pt(tpbp)) presented a NIR emission
178 spectrum centered at 765 nm with a FWHM of ~35 nm and a EQE of 6.3% (*J*=0.1 mA cm⁻²)⁴⁹.
179 However, porphyrin-based phosphors, typically suffer from efficiency roll-off due to the long-lived
180 triplet exciton resulting in self-quenching. Lanthanide phosphors, such as europium (Er(III)) and
181 niobium (Nd(III)), also exhibit NIR emission bands at the 800-1600 nm spectral region. They originate
182 from efficient energy transfer from the triplet states of the organic ligand to the *4f* states of the
183 lanthanide core and radiative recombination therefrom. However, the fabricated OLEDs achieved poor

184 EQEs not exceeding 0.15%⁵⁰. OLEDs based on a rubrene singlet fission sensitizer blended with a
185 phosphorescence emitter (termed as ErQ₃) have also achieved NIR emission centred at 1530 nm²⁰.

186

187 **The emergence of NIR perovskite light-emitting diodes**

188 Metal halide perovskites exhibit an AMX₃ chemical structure (Fig. 3a), where A is a monovalent cation
189 (organic, such as methyl ammonium, MA, and formamidinium, FA, or inorganic like cesium, Cs, or
190 their combination), M is a divalent metal such as lead (Pb²⁺) or tin (Sn²⁺), and X is a halide (Cl⁻, Br⁻, I⁻).

191 Their advantages for light-emitting applications include facile bandgap tunability through chemical
192 composition, high defect tolerance, symmetric and narrow emission spectra (FWHM<40 nm) and high
193 carrier mobilities⁵¹; the latter is useful in achieving high brightness at low driving voltages. They can
194 access the 400 to 1100 nm NIR part of the spectrum *via* changes in composition and dimensionality⁵²⁻⁵⁶
195 (Fig. 3a,b). To optimize the performance of NIR perovskite LEDs (NIR-PeLEDs), it is important to
196 simultaneously maximize the radiative recombination *via* defect passivation while suppressing non-
197 radiative Auger recombination. Three-dimensional (3D) perovskite emitters exhibit fast electron-hole
198 dissociation which decreases the probability of radiative recombination events. Strategies pursuing the
199 confinement of charge carriers *via* dimensionality tailoring, reduction in the grain size and/or film
200 thickness and growth of perovskite nanocrystals (NCs) have been widely explored.

201 The first successful NIR-PeLED employed a thin (~15 nm) EML of a mixed HP emitter, namely
202 MAPbI_{3-x}Cl_x, sandwiched between two charge injection layers⁵⁷. The device achieved an EQE and IQE
203 of 0.76% and 3.4% (at 754 nm), respectively⁵⁸. After this following attempts aimed at increasing the
204 device performance and extending the peak emission wavelength further into the NIR. The most
205 successful approaches include the development of formamidinium-based emitters such as FAPbI₃⁵⁹⁻⁶¹,
206 Pb-based mixed quasi-two dimensional (2D)/3D perovskites^{62,63}, mixed Pb-Sn⁴⁹ and Pb-free perovskites

207 with either an organic⁵⁰, or inorganic⁶⁴, cation at A-site and 2D perovskites^{65,66}. Partial or complete
208 replacement of the M-site cation, i.e., Pb²⁺ (ionic radius=1.19 Å), with alternative metals, such as Sn²⁺
209 and germanium (Ge²⁺) characterized by smaller ionic radii (1.02 Å and 0.73 Å, respectively), reduced
210 the bandgap and red shifted the emission. For example, systematic replacement of Pb²⁺ with Sn²⁺ in
211 MAPb_{1-x}Sn_xI₃ perovskites extended the emission peak from 750 nm (for x=0) to ~950 nm (x=0.8)⁵⁰. The
212 EML, stabilized by incorporating a large cation, e.g., 4-fluorobenzylammonium iodide (FPMAl),
213 exhibited an EQE of 5% (at ~917 nm). A longer NIR emission (at 950 nm) with an EQE of 3.8% was
214 reported for CsSnI₃ perovskite⁶⁷.

215 Point defects present in the polycrystalline films, such as A- and X-site vacancies, interstitials and
216 Pb-X anti-sites, act as non-radiative recombination centres and require passivation approaches to
217 suppress electronic trap states and increase ϕ_{PL} close to unity for efficient NIR-PeLEDs⁵⁸⁻⁶¹. This can be
218 accomplished through the incorporation of passivation agents (PAs) into the precursor solution or *via*
219 post-deposition treatments. Effective passivation materials contain functional groups for coordination to
220 undercoordinated Pb²⁺ or halide ions or ionic bonding to neutralize charged defects⁶⁷. They include
221 Lewis acid and base moieties, alkali metal ions, charged organic components, etc. For example, a
222 breakthrough was achieved by introducing amino-acid additives into the FAPbI₃ precursor solutions⁵⁸.
223 These additives passivated surface defects and reduced non-radiative recombination, increasing ϕ_{PL} to
224 ~70%. Moreover, they led to the spontaneous formation of submicrometre-scale structures (Fig. 3c),
225 which improved the outcoupling efficiency and viewing angle (Fig. 3d). NIR-PeLEDs employing a 3D
226 FAPbI₃ perovskite EML achieved an EQE of 20.7% (at 803 nm, $J=18 \text{ mA cm}^{-2}$)⁵⁸. Notably, these
227 devices showed a high photon flux of $2.33 \times 10^{20} \text{ m}^{-2} \text{ s}^{-1}$ at the peak EQE. Amino-functionalized PAs
228 have also proven effective in suppressing non-radiative recombination in FAPbI₃ perovskites⁵⁹. Control
229 over the hydrogen bonding between the functional moieties of the PA and the organic cation of

230 perovskite led to a record EQE of 21.6% for NIR PeLEDs (at 800 nm, ϕ_{PL} of 65%, radiance of 308 W
231 $\text{sr}^{-1} \text{m}^{-2}$, $J = 15.8 \text{ mA cm}^{-2}$).

232 Improvements in NIR-PeLEDs have also been accomplished using mixed 2D/3D domains that lead
233 to an electron-hole confining cascaded energy landscape (Fig. 3b). Therein, the carrier population is
234 funneled within a few picoseconds to the lowest bandgap domains and remains confined therein such
235 that radiative recombination and EL emission increase^{62,63}. The spatial and energy distribution of the
236 different domains within the perovskite films is crucial to maximize a homogeneous energy funnelling
237 to the lowest bandgap light emitting domains. Addition of 1-naphthylmethylamine iodide (NMAI) into a
238 perovskite precursor solution (FAI:PbI₂) resulted in the formation of multiple quantum wells (MQWs)
239 through self-organization⁶². The MQW-based LED exhibited an EQE of 11.7%. This performance
240 originated from highly confined charge carriers within the lower bandgap light-emitting 3D regions by
241 the higher bandgap (2D) regions of the perovskite MQWs. The efficiency of this 2D/3D system was
242 further improved by blending a small fraction of an insulating polymer into the perovskite EML -a
243 technique that has been able to simultaneously reduce non-radiative defects and the refractive index of
244 the perovskite film⁶³. The latter also led to an enhanced light outcoupling from PeLEDs. A device using
245 a quasi-2D/3D perovskite ((NMA)₂(FA)Pb₂I₇) blended with an insulating polymer (poly(2-hydroxyethyl
246 methacrylate, PHEMA)) showed an EQE of 20.1% ($\phi_{\text{PL}}=96\%$, EL $\sim 795 \text{ nm}$, $J=0.1 \text{ mA cm}^{-2}$)⁶³,
247 representing the best performance 2D/3D HP-based NIR-PeLEDs.

248 Colloidal HP NCs, pristine⁶⁸⁻⁷⁰ or metal-doped⁷¹⁻⁷⁴, have recently attracted attention due to their
249 advantages of quantum confined emission and low defect density with no shell passivation
250 requirements⁶⁸. NIR-PeLEDs based on FAPbI₃ NCs exhibited peak emission at 780 nm with an EQE of
251 2.3%⁶⁹, whereas those using Cs_xFA_{1-x}Pb(Br_{1-y}I_y)₃ NCs exhibited a narrow (FWHM $\sim 27 \text{ nm}$) NIR
252 emission at 735 nm with an EQE of 5.9%⁷⁰. In another approach, blend EMLs consisted of FAPbI₃ NCs

253 embedded in a molecular matrix that also served as the electron-transporting layer namely 4,4'-
254 diaminodiphenyl sulfone (DDS). In this so-called perovskite-molecule composite (PMC) approach⁶⁰, the
255 DDS matrix effectively controlled the nucleation process of the perovskite NCs, leading to the formation
256 of PMC thin films with ϕ_{PL} approaching 90% (Fig. 3e-g). NIR-PeLEDs with PMC EML achieved an
257 EQE of 17.3% (at 805 nm). Notably, the hybrid perovskite:metal NCs can achieve deeper NIR emission
258 as they rely on energy transfer from the perovskite to the metal and emission therefrom⁷³. As an
259 example, ytterbium (Yb^{3+})-doped CsPbCl_3 NCs showed NIR emission at 984 nm (EQE of 5.9%)⁷⁴.

260

261 **Progress in NIR QD light-emitting diodes**

262 Colloidal QDs are inorganic semiconductor NCs with emission properties that can be widely tuned
263 through size control due to the quantum confinement effect⁷⁵. They are prepared by wet chemical
264 synthetic procedures that offer precise control over shape and size, which allows them to access the
265 whole NIR spectrum. Their emission tunability can be achieved through increase size and compositional
266 engineering (Fig. 4a)⁷⁶. Lead chalcogenide QDs such as lead sulfide (PbS), selenide (PbSe) and telluride
267 (PbTe), pristine or capped, dominate the NIR applications⁷⁷⁻⁷⁹. NIR emission from silicon (Si) QDs has
268 been also observed⁸⁰. The appropriate selection of a wider bandgap inorganic semiconductor shell
269 epitaxially grown around the emissive QD leads to core-shell structures with significantly increased
270 exciton's binding energy⁸¹. In these structures the electron wavefunction is shifted away from the
271 surface to the QD core reducing non-radiative recombinations. Organic ligands also decorate the core-
272 shell structure (Fig. 4a, inset) to enable solubility in a large variety of non-polar solvents and offer
273 additional surface passivation⁸².

274 In spite of the development of a large variety of NIR emissive QD species, the efficiency of NIR-
275 QDLEDs had been low. This was caused by self-quenching of QDs in the solid state leading to low ϕ_{PL}

276 in thin-films combined with moderate carrier mobilities caused by the insulating organic ligands. Auger
277 recombinations are also high in QDs. To mitigate the self-quenching limitation, the first successful NIR-
278 QDLEDs employed EMLs consisted of QDs dispersed into an organic medium or forming a monolayer
279 embedded between two organic interlayers. The operation of these hybrid devices was based on exciton
280 formation in the organic host/surrounding interlayers followed by Förster energy transfer (FRET) to the
281 QDs by means of dipole-dipole interaction. The ϕ_{PL} of the EML depended critically on this energy
282 transfer step, which should compete against radiative and non-radiative recombination pathways prior
283 to energy transfer. Additionally, the performance of these devices was limited by the low mobility of the
284 organic medium/surrounding interlayers and the lack of materials with suitable energetics to enhance
285 charge injection⁸³⁻⁸⁶. For example, the first demonstration of a NIR-QDLED was based on core-shell
286 indium arsenide-zinc selenide (InAs-ZnSe) QDs embedded into a poly[2-methoxy-5-(2-ethylhexyloxy)-
287 1,4-phenylenevinylene] (MEH-PPV) matrix⁸³. The devices exhibited emission from 1000 to 1300 nm,
288 albeit with low EQE <0.5%.

289 A breakthrough in NIR-QDLEDs was achieved through the realization of devices using pristine QD-
290 based thick (~40-50 nm) EMLs⁸⁷. Herein, excitons are directly generated on the emissive QDs, thus
291 enhancing the radiative recombination rates. In addition, the charge injection efficiency was separately
292 optimized using appropriate charge-transporting layers. As a result, a device using a neat PbS EML
293 exhibited a maximum EQE of 1.15% (at 1200 nm), representing a significant improvement over
294 previous reports. A further enhancement in NIR-QDLEDs performance was achieved through the
295 precise length control of the organic ligands of PbS QDs⁸⁸. An optimized length of these ligands enabled
296 the simultaneous enhancement in radiative recombinations and carrier mobility in the QD films.
297 Appropriate interlayers injected charges directly to QDs allowing for exciton formation therein and
298 preventing their direct contact with the electrodes, thereby avoiding plasmonic quenching. As a result,

299 an EQE of ~2% (at 1054 nm, $J = 1.0 \text{ mA cm}^{-2}$) was obtained. An interlayer engineering approach was
300 also employed in the first reported Si QD NIR-LEDs, which displayed an EQE of 8.6% (at ~850 nm,
301 $J=0.01 \text{ mA cm}^{-2}$)⁸⁹.

302 Some heavy metal-free QDs are considered promising for biological applications. These are either
303 binary, such as silver (Ag) sulfide, selenide and telluride (Ag_2S , Ag_2Se , Ag_2Te), indium phosphide and
304 arsenide (InP , InAs), or ternary copper (Cu) or Ag based materials (CuInSe_2 , CuInS_2 , AgInS_2 , AgInSe_2)
305 with tunable fluorescent properties and emission maxima up to 1400 nm⁹⁰. However, the reported
306 efficiencies of the fabricated NIR-QDLEDs had been low (<0.5 %⁸³). Recently, an efficient heavy
307 metal-free NIR-QDLED was demonstrated using a giant shell $\text{In(Zn)As-In(Zn)P-GaP-ZnS}$ QD
308 emitter⁹¹. Strongly luminescent QDs were prepared through a continuous injection methodology, which
309 enabled a high ϕ_{PL} of 75% and NIR-LEDs with EQEs of 4.6% (at 857 nm, $J = 1.5 \text{ mA cm}^{-2}$). Notably,
310 LEDs with high power and large spectral bandwidth based on InAs/GaAs QDs have also been
311 reported⁹². They achieved strong emission at ~1255 nm, with a maximum output power of 2.6 mW at
312 room temperature.

313 Despite great progress in pristine QD-based NIR-LEDs, optimizing radiative recombination and
314 charge injection/transport simultaneously in these devices is challenging due to their wide bandgap
315 inorganic shells and long-chain organic ligands, which impede carrier transport in the neat QD film⁹³⁻⁹⁸.
316 Recently, this issue was successfully addressed by following a QD-in-perovskite approach using hybrid
317 EMLs consisting of QD emitters evenly distributed in a perovskite transport medium^{99,100}. Unlike prior
318 approaches, where QDs were either enclosed in a protective shell and/or insulating ligand or dispersed in
319 a low mobility organic medium, here, PbS QDs were embedded in a high mobility $\text{MAPbI}_x\text{Br}_{3-x}$
320 perovskite matrix, which epitaxially grew around the QD surface also acting as an efficient surface
321 passivation agent. This hybrid system benefitted from the high ϕ_{PL} of QDs and the superior carrier

322 mobility of the perovskite medium. The halide ratio in the perovskite was finely tuned in order to avoid
323 lattice mismatch leading to defect sites that would act as traps for non-radiative recombination (Fig.
324 4b,c)⁹⁹. QD-in-perovskite LEDs achieved 150×higher EQE (5.2%, emission peak at 1391 nm) and
325 15×higher brightness ($2.6 \text{ W sr}^{-1} \text{ m}^{-2}$ at 3.5 V) than a control QD-only LED.

326 This approach was further optimized through the incorporation of PbS QDs in a low-
327 dimensional layered perovskite¹⁰¹. The number of perovskite repeated units $\langle n \rangle$ confined between bulk
328 organic cations determined the bandgap and exciton binding energy of the resultant QW. This allowed
329 transitioning from a fully excitonic character ($n = 1, 2$) to a mixed scenario where free charges and
330 excitons coexist ($n > 2$). This was leveraged to manipulate energy transfer into the QDs achieving
331 balanced charge transport into the QD emitters and hence minimizing Auger recombination. The devices
332 achieved tunable emission in the 980-1600 nm spectral region with a maximum EQE of 8.1% (at
333 980 nm, $J = 1.65 \text{ mA cm}^{-2}$, radiance of $7.4 \text{ W sr}^{-1} \text{ m}^{-2}$). In another case, non-toxic silicon dioxide (SiO₂)-
334 encapsulated Ag₂S QDs were epitaxially dispersed in a caesium-containing triple cation perovskite
335 matrix¹⁰². The optimized NIR-LEDs demonstrated an EQE of 17.0% (at 1397 nm, $J = 11.28 \text{ mA cm}^{-2}$),
336 originating from charge balance close to unity enabled by a thin porphyrin hole-transporting interlayer
337 that also protected the perovskite matrix from metal oxide (i.e., molybdenum oxide)-induced
338 degradation.

339 A different approach employed an EML that comprised of a ternary blend including a binary
340 host matrix and the QD emitters. This matrix consisted of small size, wide bandgap PbS QDs that
341 electronically passivated the larger size, low bandgap PbS QD emitters blended with zinc oxide (ZnO)
342 NCs to balance carrier supply¹⁰³. The larger size emitters exhibited reduced non-radiative recombination
343 rates and balanced charge injection (Fig. 4d-f). The fabricated QDLEDs showed a peak emission at
344 1400 nm with an EQE of ~7.9%, which is the highest reported value for any NIR-QDLED based on a

345 neat QD EMLs. The same authors have recently achieved a higher EQE of 8.0% through further
346 engineering at the supra-nanocrystalline level and optimization of charge carrier balance within the
347 device¹⁰⁴.

348

349 **Comparison between different solution-processed NIR LEDs**

350 OLEDs and PeLEDs have already achieved high EQEs over 20% at wavelengths <1000 nm whereas
351 QDLEDs can span a larger part of the NIR spectrum with emission up to 1500 nm, albeit with lower
352 efficiencies (Fig. 5a, Supplementary Table 1). Metal halide perovskites and QDs generally enable
353 response speeds of ~ 100 ns^{105,106}, whereas OSCs based on CT states have reached response times of 14.7
354 ns¹⁰⁷. However, hybrid perovskite-polymer materials have reached high speeds of 5 ns¹⁰⁸, whereas QDs
355 recently attained an ultra-fast response of 74 ps (FWHM)¹⁰⁹, by allowing carriers to be swept to the
356 electrodes before they fall into the band tail states; these values indicate that these solution-based
357 semiconductors will be soon appropriate for NIR-applications with high speed requirements. Device
358 engineering and the design and development of novel emitters have played a crucial role to reach such
359 performance.

360

361 **Interface engineering and light outcoupling approaches**

362 The aforementioned classes of NIR-LEDs require similar architectural design considerations that mainly
363 target the reduction of charge-injection barriers, blocking of carrier leakage, and exciton confinement
364 within the EML. They have all benefitted from a rich knowledge gathered through progress in visible
365 OLEDs from which they have borrowed charge-transporting interlayers, such as organic small
366 molecules, polymers and metal oxides with appropriate energy landscapes. Extra caution, however,
367 should be paid as physicochemical interactions between these materials and novel emitters, for example,

368 perovskite ones, may negatively impact on the device performance and reliability¹¹⁰. Besides high
369 efficiency, other device performance metrics such as EQE-roll-off and operational lifetime are improved
370 through interface engineering as explained in the next sections.

371 Light trapping is a critical factor that restricts the thin-film LEDs efficiency. For example, the
372 high EQE of GaAs NIR-LEDs ($\sim 72\%$ ⁶) would be $<5\%$ without the application of complex mirror
373 structures to extract light in the viewing angle. The low outcoupling efficiency of thin-film LEDs is due
374 to the waveguide modes in the multilayered sandwich structures and plasmonic quenching at the
375 metallic electrode. In addition, the photon reabsorption by the EML and the low transmittance of
376 indium-tin-oxide (ITO) transparent electrode also contribute to efficiency losses. The waveguide modes
377 have the major contribution in light propagation losses; they divide into the glass total internal reflection
378 and the ITO/functional layers guided mode. They are regulated by Snell's law according to the refractive
379 indices of the EML (i.e., 1.7-2.0 for OSCs¹¹¹, and >2.0 for perovskites and QDs^{111,112}), ITO (~ 2.0), glass
380 substrate (1.5) and ambient air (1.0), with the η_{out} of these devices to be limited at 20-25%. Due to the
381 high refractive indices of perovskites and QDs compared with those of the substrate and the commonly
382 used charge-transporting interlayers, a large portion of the generated light is confined in the EML and
383 propagates in the lateral direction, which further compromises η_{out} .

384 To enhance light-outcoupling, numerous low-cost methods have been advanced, including patterned
385 or roughened substrates using wet-etching methods or insertion of low-index materials on the
386 substrate/air interface to extract substrate modes, low-index grids and index-matched functional layers
387 for extracting waveguide modes and corrugated metal electrodes for plasmonic modes¹¹¹. However,
388 adopting simpler methods such as manipulating the emitter's morphology¹¹³, inducing spontaneous
389 formation of submicrometre-scale structures⁵⁸, enhancing horizontal orientation of emissive dipoles⁴⁶,
390 applying cavity engineering and top emitting devices^{114,115}, using small-thickness emissive layers¹¹⁶,

391 tuning the width in MQW structures^{111,114} or enhance photon-recycling¹¹⁷, can beneficially influence
392 light extraction without increasing device fabrication cost and complexity.

393

394 **Low power output, EQE roll-off and lifetime in solution-processed NIR LEDs**

395 To meet the technical specifications of III-V LEDs for commercial applications, these solution-
396 processed NIR-LEDs need a stable power output of ~10-100 mW for $\lambda < 1000$ nm and up to several mW
397 for $\lambda > 1200$ nm (at a J of 1000-2000 mA cm⁻²). For example, for surveillance or night vision applications
398 (850-900 nm) the requirements are for a power output of 10-100 mW, which is equivalent to an
399 irradiance of 10³-10⁴ mW cm⁻². For bio-imaging in the first and second biological windows (Fig. 1a), the
400 requirements are for 10-100 mW cm⁻² dependent on the wavelength of interest. The recent developments
401 in all three classes of the solution-processed NIR-LEDs indicate that these devices will soon have the
402 potential for applications with lower power output demands such as bioimaging.

403 Another major issue in all LED technologies is the drop of EQE at high J , the so-called EQE roll-off,
404 which has been generally attributed to charge imbalance, field-induced quenching of luminescence,
405 Auger recombination and Joule heating¹¹⁸. The significant EQE-roll-off also indicates that these devices
406 are subjected to increased electrical stress to achieve a given radiance, which in-turn reduces the useful
407 lifetime; that is the time after which the radiance (or EQE) drops below a predefined level. In OLEDs, in
408 particular, as the carrier concentration increases, the bound electron-hole pairs or excitons get
409 annihilated¹¹⁹ and EQE typically drops at $J > 100$ mA cm⁻². Apart from these reasons, notable underlying
410 processes for such efficiency loss are singlet-triplet and triplet-triplet annihilation, as well as host-
411 induced quenching (in doped OLEDs)¹²⁰. Through careful design of novel emitters, judicious
412 engineering of the host-guest system and adoption of non-doped EMLs based on J -aggregated emitters,
413 suppression of various inherent loss processes has been achieved. We note, the exceptional examples of

414 NIR-OLEDs based on the boron difluoride curcuminoid TADF emitter³², or on Pt(II) complexes
415 forming J -aggregates⁴⁰, which showed negligible EQE roll-off for J values up to 700 and 500 mA cm⁻²,
416 respectively (Fig. 5b). Moreover, OLEDs have demonstrated moderate lifetime of $\times 100$ -1000 h,
417 however, at $J < 50$ mA cm⁻² (Figure 5c,d, Supplementary Table 2). Notorious reasons for low lifetime are
418 exciton quenching mechanisms explained above, presence of impurities in the EML, appearance of dark
419 spots, oxidation, corrosion, and electrochemical degradation all caused by the attack of moisture¹²¹.
420 Besides successful encapsulation, device engineering targeting to alleviate exciton quenching and
421 broaden the emission zone significantly boosts operational stability²⁴. For example, incorporation of
422 diketopyrrolopyrrole emitters in a polymer medium demonstrated OLEDs with improved durability¹¹⁹.
423 Nevertheless, the device stability will need to be improved to enable practical applications (> 10000 h
424 depending on the type of application). Encouraging in these regards are the OLEDs using wide bandgap
425 perovskite charge-injection interlayers¹²².

426 QDLEDs suffer from severe EQE roll-off¹⁰³ (Fig. 5b), which originates, apart from charge injection
427 imbalance and Auger recombination rates, by the formation of electric-fields inside the QDs known as
428 quantum-confined stark effect (QCSE)¹²³. This causes a red shift of the exciton emission
429 energy accompanied with a strong separation of electron-hole wavefunctions that dramatically decreases
430 luminescence efficiency. When QDs are dispersed in a high mobility perovskite matrix this phenomenon
431 is suppressed due to increase in the carrier density that screens the QD field. Reduced Auger
432 recombination is also expected in the QD-in-perovskite architecture due to the epitaxial passivation
433 provided by the perovskite matrix and reduced energetic disorder, ultimately promoting radiative decay
434 pathways¹²⁴. For example, the incorporation of PbS QDs in a quasi-2D perovskite EM¹⁰¹ has been
435 reported to result in balanced charge injection up to high currents nearing $J = 170$ mA cm⁻². The devices
436 showed a maximum EQE of $\sim 8\%$ and threshold current density (J_0 , corresponding to 50% EQE drop)

437 approaching 400 mA cm^{-2} . This approach has also led to improved operational stability as the main
438 device degradation mechanisms have been alleviated (Fig. 5c,d). QDLEDs using a binary blend of small
439 and large-size PbS QDs exhibited an estimated T_{50} of more than 26000 h (at initial radiance of 1 W sr^{-1}
440 m^{-2})¹⁰⁴, paving the way for durable QDLEDs operating at low brightness.

441 Perovskites possess high carrier mobilities compared to OSCs and QDs which implies that charges
442 are spread uniformly in the EML even at higher J , mitigating Auger recombination¹²⁵. Therefore, NIR-
443 PeLEDs show a lower EQE roll-off and a J_0 between $300\text{-}1500 \text{ mA cm}^{-2}$. For example, PeLEDs
444 employing a 3D perovskite $\text{Cs}_{0.17}\text{FA}_{0.83}\text{PbI}_{2.5}\text{Br}_{0.5}$ with an excess of FAI as the EML showed an EQE of
445 17.4% with a negligible roll-off up to $J=600 \text{ mA cm}^{-2}$ (Fig. 5b)⁶¹. Similarly, PeLEDs based on 2D
446 perovskites retained a nearly stable EQE for $J=1500 \text{ mA cm}^{-2}$ (Fig. 5b)⁶⁵. The observed EQE roll-off in
447 these devices is due to Joule heating, a mechanism that is more critical for PeLEDs than for other types
448 of LEDs. In fact, even small temperature changes significantly affect the device efficiency and induce
449 severe EQE roll-off¹¹⁶. Joule heating originates from inefficient charge injection into the EML,
450 conductivity mismatch between the perovskite and charge-transporting interlayers and poor perovskite
451 film morphology that can increase series resistance. Selecting suitable interlayers pristine or doped^{126,127},
452 optimizing the device geometry, using sapphire substrates to better dissipate heat or attaching heat
453 spreaders and sinks, downscaling the device active area or driving these LEDs with current pulses are
454 few of the adopted thermal management strategies^{128,129}. For example, through employing a polymer
455 hole-transporting layer with high ionization energy, large-area (900 mm^2) NIR PeLEDs emitting at 799
456 nm with a high EQE of 12.1% (EQE of small area devices 20.2%), were successfully demonstrated¹²⁷.
457 Higher lifetime is generally accomplished in pure-phase 2D, mixed phased 2D/3D and passivated 3D
458 PeLEDs where mobile ions and defects are significantly suppressed¹³⁰⁻¹³³. Alleviating Joule heating and
459 interface degradation^{132,134} has prolonged PeLEDs lifetime considerably.

460

461 **Issues with some of the emitters**

462 The presence of toxic elements, such as Pb in HPs and Cd in QDs¹³⁵, and high costs of noble metals in
463 phosphorescent complexes, raises concerns about the suitability of such materials for consumer
464 electronics. The European Restriction of Hazardous Substances Directive (RoHS) has set strict rules
465 about the use of toxic elements in electronic equipment. The current limit is 1000 ppm for Pb and 100
466 ppm for Cd by weight of solid device components. Commercially available QD TV displays use QD
467 quantities within the RoHS limits (a 55-inch display requires about 1.5 mg of Cd). This will also stand
468 for perovskites which possess identical extinction coefficient (of the order of $10^5 \text{ cm}^{-1} \text{ M}^{-1}$) with QDs
469 and similar ϕ_{PL} at the same emission wavelengths (530 and 630 nm). Although efforts to find
470 environmentally benign alternatives are also underway, up to now OLEDs based on fluorescent and
471 TADF emitters are the elective choice for *in vivo* biomedical applications, where the material's low
472 toxicity is an advantage.

473

474 **Outlook and future directions**

475 The inherent suitability of solution-processed semiconductors for large area applications allows
476 unparalleled design freedom in developing novel concepts in illumination systems. As highlighted in
477 this review, large progress in the development of narrow bandgap emissive materials and device
478 engineering has already been accomplished in recent years leading to high-performance solution-
479 processed NIR-LEDs. Primary challenges still remain in terms of high radiance, especially in the longer
480 wavelength range, and long operation stability.

481

482 **Challenges associated with pristine emitters-Towards hybrid materials?**

483 From a material engineering point of view, synthetic approaches have recently contributed towards the
484 improved device performance as they led to emitters with radiative efficiency approaching unity.
485 However, intrinsic material limitations pose restrictions on how much the bandgap of OSCs and HPs can
486 be effectively decreased constituting their emission efficient for wavelengths up to 1000 nm for the
487 former and below 900 nm for the latter class. QDs can efficiently span most of the NIR spectrum
488 through the size confinement effect; albeit with lower efficiencies.

489 Appropriate manipulation in the chemical design of OSCs and chromophores has led to some
490 notable performance levels in OLEDs in the 700-1000 nm wavelength region. Extending their
491 luminescence into the IR can be pursued by the design of molecules possessing a shallow potential
492 energy surface (PES) in their ground state, so that non-radiative recombinations originating from high-
493 frequency vibrational quenching would be significantly suppressed. Alternatively, *J*-aggregated emitters
494 allowing long wavelength emission from CT states also offer a viable path to significantly red shift the
495 emission wavelengths without compromising the device efficient and stable operation.

496 Perovskites show high performance levels with narrow emission spectra, albeit at shorter
497 wavelengths in the NIR region. Control over their composition/dimensionality raises the prospect of
498 further expanding their luminescence efficiency. Moreover, most of the passivation methods applied to
499 tackle the high defect density issue were borrowed from the solar cell research community using trial-
500 and-error approaches. With the increased demand for extended stability, these approaches are now
501 starting to reach their limits such that future major advances will require new methodologies that can
502 analyse the material and device characteristics and establish useful guidelines for rational device
503 optimization.

504 The unique optical properties of colloidal QDs have motivated an early surge of interest for their
505 application in NIR-LEDs. However, the low carrier mobility of thin-film QDs has precluded the

506 achievement of high-performance. The recently proposed ternary QD and QD-in-perovskite hybrid
507 solutions offer a promising path to overcome this limitation, enabling QDLEDs with performance
508 metrics similar to those of OLEDs and PeLEDs at much longer wavelengths. These hybrid approaches
509 are characterized by the simultaneous achievement of high mobility and enhanced non-radiative
510 recombination rates not observed in independent QD emitters. Therefore, the hybrid systems offer all the
511 advantages of individual counterparts, including the long wavelength emission, and are likely to play a
512 central role in the next generation of NIR-LEDs.

513 The hybrid materials can indeed create functionalities that couldn't have been possible otherwise.
514 Apart from the QD-in-perovskite approach, the perovskite-organic molecule composite represents a nice
515 example of how to overcome the weaknesses and strengthen the advantages of individual components to
516 some extent. In the same direction, could be the implementation of high mobility ambipolar perovskite
517 host matrices combined with *J*-aggregated or open-shell OSCs to alleviate constraints relative to poor
518 charge mobility of the latter. Inclusion of perovskite single crystals into conjugated polymer matrices to
519 form EMLs with a continuous transport phase or substitution of insulating ligands of QDs with high
520 mobility OSCs directly anchored onto the QD surface are some examples that might offer viable future
521 solutions. An added advantage to these hybrid materials is offered from the inherent solution-
522 processability of the individual components that facilitates their easy integration into devices and
523 systems to eventually transform present materials and prototypes into a promising technology.

524

525 **Limitations associated with the device design and operation**

526 From the device engineering point of view, significant progress has already been made based on
527 advances in charge-transporting interlayers developed for the more mature visible emitting OLED and
528 QDLED technologies. However, extra caution is needed prior to the application of conventional and

529 novel interfacial materials in devices embedding HPs due to the suspected physicochemical interaction
530 at the heterointerfaces. Moreover, since the commonly used ITO transparent electrode presents high
531 absorption in the NIR, considering its replacement with alternative electrodes, such as silver
532 nanowires¹³⁶, will offer advantages with respect to high efficiency and cost-effectiveness.

533 Challenges remain when targeting high and stable power output. Significant efficiency roll-off at
534 elevated J and moderate lifetimes below the 10000 h target remain key obstacles prior to the
535 commercialization of these devices. Besides the design of novel emitters, ingenious device engineering,
536 suitable encapsulation, successful management of thermal and electrical stress will prolong the device
537 lifespan considerably as they successfully counter the intrinsic and extrinsic degradation mechanisms.
538 To conclude, LEDs based on OSCs, HPs and QDs pristine and hybridized are suitable for many
539 established and emerging NIR lighting applications. There are of course important challenges ahead. As
540 research continues to progress both in the development of novel emitters and devices, we can expect
541 even more advanced performances through deepen physical understanding and optimization of each
542 technology combined with fruitful interactions and increased influence between them.

543

544 REFERENCES

- 545 1. Gu, Y. Y. et al. High-sensitivity imaging of time-domain near-infrared light transducer. *Nat.*
546 *Photonics* **13**, 525–531 (2019).
- 547 2. Smith, A. M., Mancini, M. C. & Nie, S. Second window for in vivo imaging. *Nat. Nanotechnol.*
548 **4**, 710–711 (2009).
- 549 3. Ramaswami, R. Optical fiber communication: from transmission to networking. *IEEE Commun.*
550 *Mag.* **40**, 138–147 (2002).

- 551 4. Wu, X. et al. Dye-sensitized core/active shell upconversion nanoparticles for optogenetics and
552 bioimaging applications. *ACS Nano* **10**, 1060–1066 (2016).
- 553 5. Mokkapati, S. & Jagadish, C. III-V compound SC for optoelectronic devices. *Mater. Today* **12**,
554 22–32 (2009).
- 555 6. Schnitzer, I., Yablonoitch, E., Caneau, C. & Gmitter, T. J. Ultrahigh spontaneous emission
556 quantum efficiency, 99.7% internally and 72% externally, from AlGaAs/GaAs/AlGaAs double
557 heterostructures. *Appl. Phys. Lett.* **62**, 131 (1993).
- 558 7. Broell, M., Sundgren, P., Rudolph, A., Schmid, W., Vogl, A. & Behringer, M. New
559 developments on high efficiency infrared and InGaAlP light emitting diodes at OSRAM opto-
560 semiconductors. *Proc. of SPIE* **9003**, 90030L (2014).
- 561 8. Mao, M. et al. Broadband near-infrared (NIR) emission realized by the crystal-field engineering of
562 $Y_{3-x}Ca_xAl_{5-x}S_{ix}O_{12}:Cr^{3+}$ ($x = 0-2.0$) garnet phosphors. *J. Mater. Chem. C* **8**, 1981–1988 (2020).
- 563 9. Zhong, Y. & Dai, H., A mini-review on rare-earth down-conversion nanoparticles for NIR-II
564 imaging of biological systems. *Nano Res.* **13**, 1281–1294 (2020).
- 565 10. Liu, S., Wang, Z., Cai, H., Song, Z. & Liu, Q. Highly efficient near-infrared phosphor
566 $LaMgGa_{11}O_{19}:Cr^{3+}$. *Inorg. Chem. Front.* **7**, 1467–1473 (2020).
- 567 11. Zampetti, A.; Minotto, A. & Cacialli, F. Near-infrared (NIR) organic light-emitting diodes
568 (OLEDs): Challenges and opportunities. *Adv. Funct. Mater.* **29**, 1807623 (2019).
- 569 12. Kumawat, N. K., Dey, A., Narasimhan, K. L. & Kabra, D., Near infrared to visible
570 electroluminescent diodes based on organometallic halide perovskites: structural and optical
571 investigation. *ACS Photonics* **2**, 349–354 (2015).
- 572 13. Sargent, E. H., Infrared quantum dots. *Adv. Mater.* **17**, 515–522 (2005).

- 573 14. Mikhnenko, O. V., Blom, P. W. M. & Nguyen, T.-Q. Exciton diffusion in organic
574 semiconductors. *Energy Environ. Sci.* **8**, 1867–1888 (2015).
- 575 15. Voznyy, O., Sutherland, B. R., Ip, A. H., Zhitomirsky, D. & Sargent, E. H. Engineering charge
576 transport by heterostructuring solution-processed semiconductors. *Nat. Rev. Mater.* **2**, 17026 (2017).
- 577 16. Liu, X.-K., Xu, W., Bai, S., Jin, Y., Wnag, J., Friend, R. H. & Gao, F. Metal halide perovskites for
578 light-emitting diodes. *Nat. Mater.* **20**, 10–21 (2021).
- 579 17. Zhang, Y. et al. Near-infrared emitting materials *via* harvesting triplet excitons: Molecular design,
580 properties, and application in organic light emitting diodes. *Adv. Opt. Mater.* **6**, 1800466 (2018).
- 581 18. Uoyama, H., Goushi, K., Shizu, K., Nomura, H. & Adachi, C. Highly efficient organic light-
582 emitting diodes from delayed fluorescence. *Nature* **492**, 234–238 (2012).
- 583 19. Adachi, C. Third-generation organic electroluminescence materials. *Jpn. J. Appl. Phys.* **53**, 060101
584 (2014).
- 585 20. Nagata, R., Nakanotani, H., Potscavage Jr., W. J. & Adachi, C. Exploiting singlet fission in
586 organic light-emitting diodes. *Adv. Mater.* **30**, 1801484 (2018).
- 587 21. Narsaria, A. K., Poater, J., Guerra, C. F., Ehlers, A. W., Lammertsma, F. M., Rational design of
588 near-infrared absorbing organic dyes: Controlling the HOMO–LUMO gap using quantitative molecular
589 orbital theory. *J. Comput. Chem.* **39**, 2690–2696 (2018).
- 590 22. Roncali, J. Molecular engineering of the band gap of π -conjugated systems: facing technological
591 applications. *Macromol. Rapid Commun.* **28**, 1761–1775 (2007).
- 592 23. Englman, R. & Jortner, J. The energy gap law for radiationless transitions in large molecules. *Mol.*
593 *Phys.* **18**, 145–164 (1970).
- 594 24. Minotto, A. et al. Efficient near-infrared electroluminescence at 840 nm with "metal-free" small-
595 molecule:polymer blends. *Adv. Mater.* **30**, 1706584 (2018).

- 596 25. Minotto, A. et al. Towards efficient near-infrared fluorescent organic light-emitting diodes. *Light*
597 *Sci. Appl.* **10**, 18 (2021).
- 598 26. Peng, Q., Obolda, A., Zhang, M. & Li, F. Organic light-emitting diodes using a neutral π radical as
599 emitter: The emission from a doublet. *Angew. Chem. Int. Ed.* **54**, 7091–7095 (2015).
- 600 27. Guo, H. et al. High stability and luminescence efficiency in donor–acceptor neutral radicals not
601 following the Aufbau principle. *Nature Mater.* **18**, 977–984 (2019).
- 602 28. Ai, X. et al. Efficient radical-based light-emitting diodes with doublet emission. *Nature* **563**, 536–
603 540 (2018).
- 604 29. Yamanaka, T., Nakanotani, H., Hara, S., Hirohata, T. & Adachi, C. Near-infrared organic light-
605 emitting diodes for biosensing with high operating stability. *Appl. Phys. Express* **10**, 074101 (2017).
- 606 30. Wang, S. et al. Highly efficient near-infrared delayed fluorescence organic light emitting diodes
607 using a phenanthrene-based charge-transfer compound. *Angew. Chem. Int. Ed.* **54**, 13068–13072 (2015).
- 608 31. Yuan, Y. et al. Over 10% EQE near-infrared electroluminescence based on a thermally activated
609 delayed fluorescence emitter. *Adv. Funct. Mater.* **27**, 1700986 (2017).
- 610 32. Kim, D. H. et al. High-efficiency electroluminescence and amplified spontaneous emission from a
611 thermally activated delayed fluorescent near-infrared emitter. *Nat. Photonics* **12**, 98–104 (2018).
- 612 33. Ye, H. et al. Near-infrared electroluminescence and low threshold amplified spontaneous emission
613 above 800 nm from a thermally activated delayed fluorescent emitter. *Chem. Mater.* **30**, 6702–6710
614 (2018).
- 615 34. Hu, Y. Yuan, Y., Shi, Y.-L., Li, D., Jiang, Z.-Q. & Liao, L.-S. Efficient near-infrared emission
616 by adjusting the guest–host interactions in thermally activated delayed fluorescence organic light-
617 emitting diodes. *Adv. Funct. Mater.* **28**, 1802597 (2018).

- 618 35. Xue, J. et al. Highly efficient thermally activated delayed fluorescence via *J*-aggregates with
619 strong intermolecular charge transfer. *Adv. Mater.* **31**, 1808242 (2019).
- 620 36. Liang, Q., Xu, J., Xue, J. & Qiao, J. Near-infrared-II thermally activated delayed fluorescence
621 organic light-emitting diodes. *Chem. Commun.* **56**, 8988–8991 (2020).
- 622 37. Congrave, D. G. et al. A simple molecular design strategy for delayed fluorescence toward 1,000
623 nm. *J. Am. Chem. Soc.* **141**, 46, 18390–18394 (2019).
- 624 38. Shahaliazad, A. et al. Efficient solution-processed hyperfluorescent OLEDs with spectrally narrow
625 emission at 840 nm. *Adv. Funct. Mater.* **31**, 2007119 (2021).
- 626 39. Brodeur, J., Hu, L., Malinge, A., Elad Eizner, E., Skene, W. G. & Kéna-Cohen, S. Highly efficient
627 and spectrally narrow near-infrared fluorescent OLEDs using a TADF-sensitized cyanine dye. *Adv.*
628 *Optical Mater.* **7**, 1901144 (2019).
- 629 40. Wei, Y. C. et al. Overcoming the energy gap law in near-infrared OLEDs by exciton–vibration
630 decoupling. *Nat. Photonics* **14**, 570–577 (2020).
- 631 41. Xue J. et al. Homoleptic facial Ir(III) complexes *via* facile synthesis for high-efficiency and low-
632 roll-off near-infrared organic light-emitting diodes over 750 nm. *Chem. Mater.* **29**, 4775–4782 (2017).
- 633 42. Lee, T.-C. et al. rational design of charge-neutral, near-infrared-emitting osmium(II) complexes
634 and OLED fabrication. *Adv. Funct. Mater.* **19**, 2639-2647 (2009).
- 635 43. Chen, Z. et al. A simple and efficient approach toward deep-red to near-infrared-emitting iridium(III)
636 complexes for organic light-emitting diodes with external quantum efficiencies of over 10%. *Chem. Sci.* **11**,
637 2342-2349 (2020).
- 638 44. Yuan, Y., Liao, J.-L., Ni, S.-F., Je, A. K.-Y., Lee, C.-S. & Chi, Y. Boosting efficiency of near-
639 infrared organic light-emitting diodes with Os(II)-based pyrazinyl azolate emitters. *Adv. Funct. Mater.*
640 **30**, 1906738 (2020).

- 641 45. Cocchi, M., Kalinowski, J., Virgili, D. & Williams, J. A. G. Excimer-based red/near-infrared
642 organic light-emitting diodes with very high quantum efficiency. *Appl. Phys. Lett.* **92**, 113302 (2008).
- 643 46. Tuong Ly, K. et al. Near-infrared organic light-emitting diodes with very high external quantum
644 efficiency and radiance. *Nat. Photonics* **11**, 63–68 (2017).
- 645 47. Chen, W.-C. et al. Modulation of solid-state aggregation of square-planar Pt(II) based emitters:
646 enabling highly efficient deep-red/near infrared electroluminescence. *Adv. Funct. Mater.* **30**, 2002494
647 (2020).
- 648 48. Wang, S. F. et al. Highly efficient near-infrared electroluminescence up to 800 nm using
649 Platinum(II) phosphors. *Adv. Funct. Mater.* **30**, 2002173 (2020).
- 650 49. Borek, C. et al. Highly efficient, near-infrared electrophosphorescence from a Pt–metalloporphyrin
651 complex. *Angew. Chem. Int. Ed.* **46**, 1109–1112 (2007).
- 652 50. Jinnai, K., Kabe, R. & Adachi, C. A near-infrared organic light-emitting diode based on an Yb(III)
653 complex synthesized by vacuum co-deposition. *Chem. Commun.* **53**, 5457–5460 (2017).
- 654 51. Sutherland, B. R. & Sargent, E. H. Perovskite photonic sources. *Nat. Photonics* **10**, 295–302
655 (2016).
- 656 52. Qiu, W. et al. Mixed lead–tin halide perovskites for efficient and wavelength-tunable near-infrared
657 light-emitting diodes. *Adv. Mater.* **31**, 1806105 (2019).
- 658 53. Lai, M. L. et al. Tunable near-infrared luminescence in tin halide perovskite devices. *J. Phys.*
659 *Chem. Lett.* **7**, 2653–2658 (2016).
- 660 54. Smith, M. D., Connor, B. A. & Karunadasa, H. I. Tuning the luminescence of layered halide
661 perovskites. *Chem. Rev.* **119**, 3104–3139 (2019).
- 662 55. Akkerman, Q. A., Rainò, G., Kovalenko, M. V. & Manna, L. Genesis, challenges and
663 opportunities for colloidal lead halide perovskite nanocrystals. *Nat. Mater.* **17**, 394–405 (2018).

- 664 56. G. Xing, *et al.* Low-temperature solution-processed wavelength-tunable perovskites for lasing.
665 *Nat. Mater.*, **13** 476–480 (2014).
- 666 57. Z.-K. Tan, *et al.* Bright light-emitting diodes based on organometal halide perovskite. *Nat.*
667 *Nanotechnol.*, **9**, 687–692 (2014).
- 668 58. Cao, Y. *et al.* Perovskite light-emitting diodes based on spontaneously formed submicrometre-
669 scale structures. *Nature* **562**, 249–253 (2018).
- 670 59. Xu, W. *et al.* Rational molecular passivation for high-performance perovskite light-emitting
671 diodes. *Nat. Photon.* **13**, 418–424 (2019).
- 672 60. Wang, H. *et al.* Perovskite-molecule composite thin films for efficient and stable light-emitting
673 diodes. *Nat. Commun.* **11**, 891 (2020).
- 674 61. Jia, Y.-H. *et al.* Role of excess FAI in formation of high-efficiency FAPbI₃-based light-emitting
675 diodes. *Adv. Funct. Mater.* **30**, 1906875 (2020).
- 676 62. Wang, N. *et al.* Perovskite light-emitting diodes based on solution-processed self-organized
677 multiple quantum wells. *Nat. Photonics* **10**, 699–704 (2016).
- 678 63. Zhao, B. *et al.* High-efficiency perovskite-polymer bulk heterostructure light-emitting. *Nat.*
679 *Photonics* **12**, 783–789 (2018).
- 680 64. Hong, W.-L. *et al.* Efficient low-temperature solution-processed lead-free perovskite infrared
681 light-emitting diodes. *Adv. Mater.* **28**, 8029–8036 (2016).
- 682 65. Yang, R. *et al.* Oriented quasi-2D perovskites for high performance optoelectronic devices. *Adv.*
683 *Mater.* **30**, 1804771 (2018).
- 684 66. Tsai, H. *et al.* Stable light-emitting diodes using phase-pure Ruddlesden–Popper layered
685 perovskites. *Adv. Mater.* **30**, 1704217 (2018).

- 686 67. Giuri, A. *et al.* Ultra-Bright Near-infrared perovskite light-emitting diodes with reduced efficiency
687 roll-off. *Sci. Rep.* **8**, 15496 (2018).
- 688 68. Kovalenko, M. V., Protesescu, L. & Bodnarchuk, M. I. Properties and potential optoelectronic
689 applications of lead halide perovskite nanocrystals. *Science* **358**, 6364, 745–750 (2017).
- 690 69. Protesescu, L. *et al.* Dismantling the “red wall” of colloidal perovskites: highly luminescent
691 formamidinium and formamidinium–cesium lead iodide nanocrystals. *ACS Nano* **11**, 3, 3119–3134
692 (2017).
- 693 70. Lignos, I. *et al.* Exploration of near-infrared-emissive colloidal multinary lead halide perovskite
694 nanocrystals using an automated microfluidic platform. *ACS Nano* **12**, 6, 5504–5517 (2018).
- 695 71. Pan, G. *et al.* Doping lanthanide into perovskite nanocrystals: Highly improved and expanded
696 optical properties. *Nano Lett.* **17**, 8005–8011 (2017).
- 697 72. Shen, X. *et al.* Zn-alloyed CsPbI₃ nanocrystals for highly efficient perovskite light-emitting
698 devices. *Nano Lett.* **19**, 1552–1559 (2019).
- 699 73. Milstein, T. J., Kroupa, D. M. & Gamelin, D. R. Picosecond quantum cutting generates
700 photoluminescence quantum yields over 100% in ytterbium-doped CsPbCl₃ nanocrystals. *Nano Lett.* **18**,
701 3792–3799 (2018).
- 702 74. Ishii, A. & Miyasaka, T. Sensitized Yb³⁺ luminescence in CsPbCl₃ film for highly efficient near-
703 infrared light-emitting diodes. *Adv. Sci.* **7**, 1903142 (2020).
- 704 75. Shirasaki, Y., Supran, G. J., Bawendi, M. G. & Bulovic, V. Emergence of colloidal quantum-dot
705 light-emitting technologies. *Nat. Photonics* **7**, 13–23 (2013).
- 706 76. Ma, Y., Zhang, Y. & Yu, W. W. Near infrared emitting quantum dots: synthesis, luminescence
707 properties and applications. *J. Mater. Chem. C* **7**, 13662–13679 (2019).

- 708 77. Rogach, A. L. et al. Colloidally prepared HgTe nanocrystals with strong room-temperature
709 infrared luminescence. *Adv. Mater.* **11**, 552–555 (1999).
- 710 78. Harrison, M. T. et al. Wet chemical synthesis of highly luminescent HgTe/CdS core/shell
711 nanocrystals. *Adv. Mater.* **12**, 123–125 (2000).
- 712 79. Harris, D. K. et al. Synthesis of cadmium arsenide quantum dots luminescent in the infrared. *J.*
713 *Am. Chem. Soc.* **133**, 4676–4679 (2011).
- 714 80. Cheng, K.-Y., Anthony, R., Kortshagen, U. R. & Holmes, R. J. Hybrid silicon nanocrystal-organic
715 light-emitting devices for infrared electroluminescence. *Nano Lett.* **10**, 1154–1157 (2010).
- 716 81. Tang, R. et al. Tunable ultrasmall visible-to-extended near-infrared emitting silver sulfide
717 quantum dots for integrin-targeted cancer imaging. *ACS Nano* **9**, 220–230 (2015).
- 718 82. Hinds, S. et al. NIR-emitting colloidal quantum dots having 26% luminescence quantum yield in
719 buffer solution. *J. Am. Chem. Soc.* **129**, 7218–7219 (2007).
- 720 83. Tessler, N., Medvedev, V., Kazes, M., Kan, S. & Banin, U. Efficient near-infrared polymer
721 nanocrystal light-emitting diodes. *Science* **295**, 1506–1508 (2002).
- 722 84. Steckel, J. S., Coe-Sullivan, S., Bulovic, V. & Bawendi, M. G. 1.3 μm to 1.55 μm Tunable
723 electroluminescence from PbSe quantum dots embedded within an organic device. *Adv. Mater.* **15**,
724 1862–1866 (2003).
- 725 85. Konstantatos, G., Huang, C. J., Levina, L., Lu, Z. H. & Sargent, E. H. Efficient infrared
726 electroluminescent devices using solution-processed colloidal quantum dots. *Adv. Funct. Mater.* **15**,
727 1865–1869 (2005).
- 728 86. Choudhury, K. R., Song, D. W. & Franky, S. Efficient solution-processed hybrid polymer-
729 nanocrystal near infrared light-emitting devices. *Org. Electron.* **11**, 23–28 (2010).

- 730 87. Bourdakos, K. N., Dissanayake, D. M. N. M., Lutz, T., Silva, S. R. P. & Curry, R. J. Highly
731 efficient near-infrared hybrid organic-inorganic nanocrystal electroluminescence device. *Appl. Phys.*
732 *Lett.* **92**, 153311 (2008).
- 733 88. Sun, L. et al. Bright infrared quantum-dot light-emitting diodes through inter-dot spacing control.
734 *Nat. Nanotechnol.* **7**, 369–373 (2012).
- 735 89. Cheng, K.-Y., Anthony, R., Kortshagen, U. R. & Holmes, R. J. High efficiency silicon nanocrystal
736 light-emitting devices. *Nano Lett.* **11**, 1952–1956 (2011).
- 737 90. Franke, D. et al. Continuous injection synthesis of indium arsenide quantum dots emissive in the
738 short-wavelength infrared. *Nat. Commun* **7**, 12749 (2016).
- 739 91. Wijaya, H. et al. Efficient near-infrared light-emitting diodes based on In(Zn)As–In(Zn)P–GaP–
740 ZnS quantum dots. *Adv. Funct. Mater.* **30**, 1906483 (2020).
- 741 92. Chen, S. et al. InAs/GaAs quantum-dot superluminescent light-emitting diode monolithically
742 grown on a Si substrate. *ACS Photonics* **1**, 7, 638–642 (2014).
- 743 93. Hu, W. et al. Near-infrared quantum dot light emitting diodes employing electron transport
744 nanocrystals in a layered architecture. *Nanotechnology* **23**, 375202 (2012).
- 745 94. Ma, X., Xu, F., Benavides, J. & Cloutier, S. G. High performance hybrid near-infrared LEDs using
746 benzenedithiol cross-linked PbS colloidal nanocrystals. *Org. Electron.* **13**, 525–531 (2012).
- 747 95. Zhitomirsky, D., Voznyy, O., Hoogland, S. & Sargent, E. H. Measuring charge carrier diffusion in
748 coupled colloidal quantum dot solids. *ACS Nano* **7**, 5282–5290 (2013).
- 749 96. Sanchez, R. S. et al. All solution processed low turn-on voltage near infrared LEDs based on core–shell
750 PbS–CdS quantum dots with inverted device structure. *Nanoscale* **6**, 8551–8555 (2014).
- 751 97. Supran, G. J., et al. High-performance shortwave-infrared light-emitting devices using core–shell
752 (PbS–CdS) colloidal quantum dots. *Adv. Mater.* **27**, 1437–1442 (2015).

- 753 98. Yang, X. et al. Iodide capped PbS/CdS core-shell quantum dots for efficient long-wavelength
754 near-infrared light-emitting diodes. *Sci. Rep.* **7**, 14741 (2017).
- 755 99. Gong, X. et al. Highly efficient quantum dot near-infrared light-emitting diodes. *Nat. Photonics*
756 **10**, 253–257 (2016).
- 757 100. Ning, Z. et al. Quantum-dot-in-perovskite solids. *Nature* **523**, 324–328 (2015).
- 758 101. Gao, L. et al. Efficient near-infrared light-emitting diodes based on quantum dots in layered
759 perovskite. *Nat. Photonics* **14**, 227–233 (2020).
- 760 102. Vasilopoulou, M. et al. Efficient colloidal quantum dot light-emitting diodes operating in the
761 second near-infrared biological window. *Nat. Photonics* **14**, 50–56, (2020).
- 762 103. Pradhan, S. et al. High-efficiency colloidal quantum dot infrared light-emitting diodes via
763 engineering at the supra-nanocrystalline level. *Nat. Nanotechnol.* **14**, 72–79 (2019).
- 764 104. Pradhan, S., Dalmases, M., Baspinar, A.-B. & Konstantatos, G. Highly efficient, bright, and stable
765 colloidal quantum dot short-wave infrared light-emitting diodes. *Adv. Funct. Mater.* 2004445 (2020).
- 766 105. Li, L. et al. Self-filtered narrowband perovskite photodetectors with ultrafast and tuned spectral
767 response. *Adv. Optical Mater.* **5**, 1700672 (2017).
- 768 106. Dortaj, S. et al. High-speed and high-precision PbSe/PbI₂ solution process mid-infrared
769 camera. *Sci Rep* **11**, 1533 (2021).
- 770 107. Ullbrich, S. et al. Fast organic near-infrared photodetectors based on charge-transfer absorption. *J.*
771 *Phys. Chem. Lett.* **8**, 22, 5621–5625 (2017).
- 772 108. Shen, L. et al. Integration of perovskite and polymer photoactive layers to produce ultrafast
773 response, ultraviolet-to-near-infrared, sensitive photodetectors. *Mater. Horiz.* **4**, 242-248 (2017).
- 774 109. Gao, J., Nguyen, S., Bronstein, N. D. & Alivisatos, A. P. Solution-processed, high speed and high
775 quantum efficiency quantum dot infrared photodetectors. *ACS Photonics* **3**, 7, 1217–1222 (2016).

- 776 110. Quan, L. N. et al. Perovskites for next-generation optical sources. *Chem. Rev.* **119**, 12, 7444–
777 7477 (2019).
- 778 111. Zhang, Q. et al. Light out-coupling management in perovskite LEDs-what can we learn from the
779 past? *Adv. Funct. Mater.* **30**, 2002570 (2020).
- 780 112. Zhang, X., Hägglund, C. & Johansson, E. M. J. Electro-optics of colloidal quantum dot solids for
781 thin-film solar cells. *Adv. Funct. Mater.* **26**, 1253-1260 (2016).
- 782 113. Xiao, Z. et al. Efficient perovskite light-emitting diodes featuring nanometre-sized
783 crystallites. *Nat. Photonics* **11**, 108–115 (2017).
- 784 114. Miao, Y. et al. Microcavity top-emission perovskite light-emitting diodes. *Light Sci. Appl.* **9**, 89
785 (2020).
- 786 115. Shen, Y. et al. High-efficiency perovskite light-emitting diodes with synergetic outcoupling
787 enhancement. *Adv. Mater.* **31**, 1901517 (2019).
- 788 116. Zhao, L., Lee, K. M., Roh, K., Khan, S. U. Z. & Rand, B.P. Improved outcoupling efficiency and
789 stability of perovskite light-emitting diodes using thin emitting layers. *Adv. Mater.* **31**, 1805836 (2019).
- 790 117. Cho, C. et al. The role of photon recycling in perovskite light-emitting diodes. *Nat. Commun.* **11**,
791 611 (2020).
- 792 118. Murawski, C., Leo, K. & Gather, M. C. Efficiency roll-off in organic light-emitting diodes. *Adv.*
793 *Mater.* **25**, 6801–6827 (2013).
- 794 119. Sassi, M. et al. Near-infrared roll-off-free electroluminescence from highly stable
795 diketopyrrolopyrrole light emitting diodes. *Sci. Rep.* **6**, 34096 (2016).
- 796 120. Bencheikh, F., Sandanayaka, A. S. D., Fukunaga, T. Matsushima, T. & Adachi. C. Origin of
797 external quantum efficiency roll-off in 4,4'-bis[(N-carbazole)styryl]biphenyl (BSBCz)-based inverted
798 organic light emitting diode under high pulsed electrical excitation. *J. Appl. Physics* **126**, 185501 (2019).

799 121. Swayamprabha, S. S. et al. Approaches for long lifetime organic light emitting diodes. *Adv.*
800 *Science* **8**, 2002254 (2020).

801 122. Matsushima, T. et al. High performance from extraordinarily thick organic light-emitting diodes.
802 *Nature* **572**, 502–506 (2019).

803 123. Titov, A. et al. 6-3: Quantum dot LEDs: Problems & prospects. *SID Symp. Dig. Tech. Pap.* **48**,
804 58–60 (2017).

805 124. Gao, Y. et al. Disorder strongly enhances Auger recombination in conductive quantum-dot
806 solids. *Nat. Commun.* **4**, 2329 (2013).

807 125. Kim, K. et al. Hybrid perovskite light emitting diodes under intense electrical excitation. *Nat.*
808 *Commun.* **9**, 4893 (2018).

809 126. Fakharuddin, A. et al. Reduced efficiency roll-off and improved stability of mixed 2D/3D
810 perovskite light emitting diodes by balancing charge injection. *Adv. Funct. Mater.* **29**, 1904101 (2019).

811 127. Zhao, X. & Tan, Z.-K. Large-area near-infrared perovskite light-emitting diodes. *Nat. Photonics*
812 **14**, 215–218 (2020).

813 128. Zhao, L. et al. Thermal management enables bright and stable perovskite light-emitting diodes.
814 *Adv. Mater.* **32**, 2000752 (2020).

815 129. Zou, C., Liu, Y., Ginger, D. S. & Lin, L. Y. Suppressing efficiency roll-off at high current
816 densities for ultra-bright green perovskite light-emitting diodes. *ACS Nano* **14**, 5, 6076–6086 (2020).

817 130. Yoshida, K., Nakanotani, H. & Adachi, C. Effect of Joule heating on transient current and
818 electroluminescence in p-i-n organic light-emitting diodes under pulsed voltage operation. *Org.*
819 *Electron.* **31**, 287–294 (2016).

820 131. Kim, H. et al. Proton-transfer-induced 3D/2D hybrid perovskites suppress ion migration and
821 reduce luminance overshoot. *Nat. Commun.* **11**, 3378 (2020).

- 822 132. Prakasam, V, Tordera, D., Bolink, H. J. & Gelinck, G. Degradation mechanisms in organic lead
823 halide perovskite light-emitting diodes. *Adv. Optical Mater.* **7**, 1900902 (2020).
- 824 133. Guo, Y. *et al.* Phenylalkylammonium passivation enables perovskite light emitting diodes with
825 record high-radiance operational lifetime: the chain length matters. *Nat. Commun.* **12**, 644 (2021).
- 826 134. Yuan, Z. *et al.* Unveiling the synergistic effect of precursor stoichiometry and interfacial reactions
827 for perovskite light-emitting diodes. *Nat. Commun.* **10**, 2818 (2019).
- 828 135. Moroz, P. *et al.* Infrared emitting PbS nanocrystal solids through matrix encapsulation. *Chem.*
829 *Mater.* **26**, 14, 4256–4264 (2014).
- 830 136. Xie, C., Zhao, X., Ong, E. W. Y. & Tan, Z.-K. Transparent near-infrared perovskite light-emitting
831 diodes. *Nat. Commun.* **11**, 4213 (2020).

832

833 **Acknowledgements**

834 M.V. acknowledges funding by the project “Development of Materials and Devices for Industrial,
835 Health, Environmental and Cultural Applications” (MIS 5002567), which is implemented under the
836 “Action for the Strategic Development on the Research and Technological Sector”, funded by the
837 Operational Programme "Competitiveness, Entrepreneurship and Innovation" (NSRF 2014-2020) and
838 co-financed by Greece and the European Union (European Regional Development Fund). H.J.B.
839 acknowledges funding from the European Research Council (ERC) under the European Union’s
840 Horizon 2020 research and innovation programme (grant agreement no. 834431) and the Spanish
841 Ministry of Science, Innovation and Universities MAT2017-88821-R and CEX2019-000919-M.
842 F.P.G.d.A. and E.H.S. acknowledge support from the Canada Research Chair.

843

844 **Competing interests**

845 The authors declare no competing interests.

846

847 **Additional information**

848 Correspondence should be addressed to M.V., H. J. B. or E. H. S.

849

850 **Supplementary Information**

851 Tables including key figure of merits and stability data of solution-processed NIR LEDs,

852

853

854

855

856

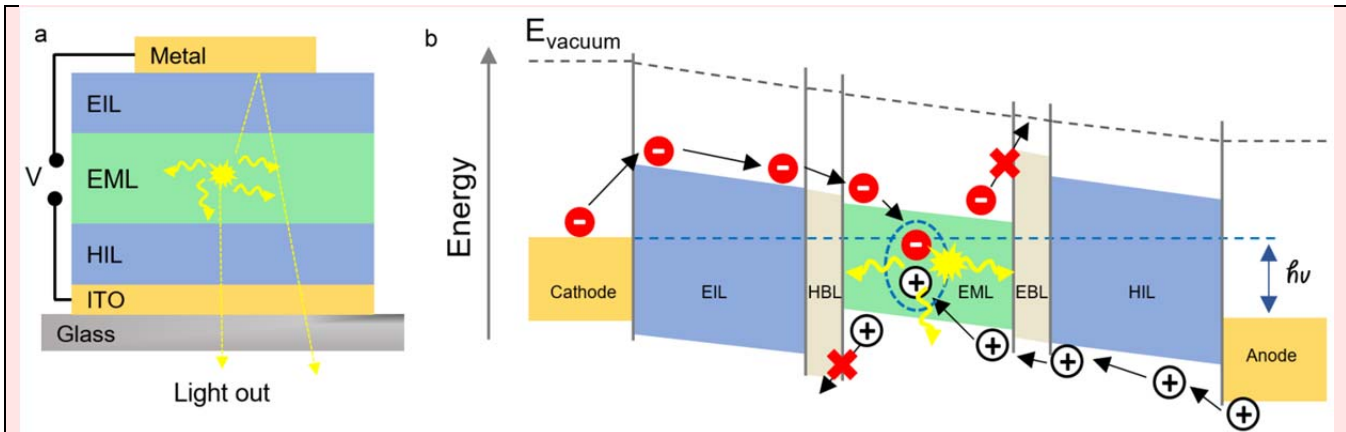
857

858

Box 1

The device architecture and key performance parameters of solution-processed NIR-LEDs

Typical solution-processed NIR-LEDs consist of a multilayer architecture, embedding the semiconductor emissive layer (EML) between an electron-injection (EIL) and a hole-injection layer (HIL), similarly to their visible emitting counterparts, as illustrated in the Scheme 1a. In some cases, appropriate interlayers are also applied to block opposite charges from leaking through the device (which are the hole blocking layer, HBL, and the electron blocking layer, EBL). Under forward bias, electrons and holes injected from the electrodes drift and diffuse within the EML (electrons are transferred to the lowest occupied molecular orbital, LUMO, of the organic emissive semiconductor or the conduction band minimum of the inorganic ones, such as perovskites and colloidal quantum dots, whereas holes are transferred towards the highest occupied molecular orbital, HOMO, or the valence band maximum of either the organic or the inorganic semiconductor, respectively, see Scheme 1b), and eventually recombine emitting photons or heat.



Scheme 1 a, Device architecture and **b**, working principle of a solution-processed LED.

The key performance parameters of a NIR-LED are the external quantum efficiency (EQE), the power density (P) or radiance, the device lifetime and efficiency roll-off. EQE denotes the ratio of emitted photons versus the injected charges under external bias and is expressed as the product of the internal quantum efficiency (IQE) and the light outcoupling efficiency (η_{out}) (Eq. 1):

$$EQE = \frac{\text{emitted photons}}{\text{injected charges}} = IQE \times \eta_{out} \quad (1)$$

The η_{out} is the outcoupling efficiency while the IQE value (Eq. 2) is proportional to the probability for radiative decay to occur (r), the photoluminescence quantum yield of the emitter (PLQY or ϕ_{PL}), and to the probability that electrons and holes recombining (γ):

$$IQE = r \times \phi_{PL} \times \gamma \quad (2)$$

Luminance is a figure of merit not relevant to NIR-LEDs thus measuring the amount of radiant intensity per unit projected area (the so-called radiance given in $W\ m^{-2}\ sr^{-1}$) is more appropriate.

The emitted light intensity or power output density (P) of an NIR-LED is important for applications, such as spectroscopy and sensing. This, is proportional to the EQE and the current density (J) (Eq. 3):

$$P = \frac{E_\nu J}{q} EQE \quad (3)$$

where EQE is derived by Eq. 1, E_ν is the energy of a photon and q is the elementary charge.

859

860

861

862 **Figure captions**

863

864 **Fig. 1 Applicability and scalability of solution-processed NIR-LEDs.** **a**, The infrared spectral region
 865 and illustration of selected applications. NIR, near-infrared; SWIR, short-wave infrared. MIR, mid-
 866 infrared; NIR sources are in demand for application in biosensing, optogenetics, biometrics, night
 867 vision, data storage, surveillance and 3D imaging. Biological transparency windows are defined as
 868 follows: first (NIR-I, 650-950 nm), second (NIR-II, 1100–1350 nm), third (NIR-III, 1600–1870 nm)
 869 and fourth (NIR-IV, centred at 2200 nm) NIR windows that allow for clearer imaging due to a scattering
 870 and absorption reduction. The telecom window between 800–900 nm was originally used for
 871 transmitting information, followed by the range 1260–1360 nm (or O-band) for short distance
 872 communication, while today the 1530–1565 nm range (known as the C-band) is the most commonly

873 used band for long haul optical transmission. **b**, Solution-processed NIR-LEDs can be processed from
874 inks using various methods as shown.

875

876

877 **Fig. 2 NIR emission from organic semiconductors.** Energy diagram depicting photophysical processes
878 for light emission: **a**, fluorescence (1), phosphorescence (2), intersystem crossing (ISC) from singlet to
879 triplet levels, and thermally activated delayed fluorescence (3), obtained upon reverse intersystem
880 crossing (RISC). **b**, Delayed fluorescence (DF) (4) due to triplet-triplet annihilation (TTA). **c**, Singlet
881 fission to two triplets (5). **d**, Molecular parameters controlling bandgap narrowing in organic
882 chromophores. **e**, Photoluminescence quantum yield (ϕ_{PL}) for different organic chromophores in relation
883 to their emission wavelength. The dashed line is guide to the eye. **f**, Electroluminescence by selective
884 HOMO and SOMO hole and electron injection. The scheme shows two routes to create D_1 (first doublet
885 excited state. $[S]$ and $[S, T_0, T_+, T_-]^+$ denote negatively and positively charged intermediates. **g**, PLQY
886 values of CBP blend films doped with the curcuminoid NIR TADF emitter (shown as inset) at various
887 concentrations. **h**, Chemical structures of Pt(II) phosphorescence complexes 1–3: $[Pt(fprpz)_2]$
888 (compound 1), $Pt(fprpz)(fppz)$ (compound 2), $[Pt(fprpz)(tbfppz)]$ (compound 3) and **i**, their normalized
889 PL spectra in thin films. Panels reproduced with permission from: **d**, ref.¹¹ Wiley-VCH; **e**, ref.²² Wiley-
890 VCH; **f**, ref.²⁸, Springer Nature Ltd; **g**, ref.³², Springer Nature Ltd; **h,i**, ref.⁴⁶, Springer Nature Ltd.

891

892 **Fig. 3 NIR light emission from perovskite LEDs.** **a**, Illustration of the crystal structure of
893 dimensionally engineered halide pure-phase ($n = 1, 2 \& 3$), mixed phase (2D/3D) and a classical
894 polycrystalline 3D perovskite. **b**, Schematic showing energy (charge) funneling from larger to smaller
895 bandgap perovskite domains. The process takes place at ultrafast timescale (ps). **c**, Formation of
896 submicrometre perovskite structure via solution processing. **d**, Photoluminescence (PL) and
897 electroluminescence (EL) spectra of the device at different viewing angles. **e-g**, Device architecture, EL
898 spectra and EQE curves of LEDs employing 3D perovskite nanocrystals embedded in an electron-
899 transport molecular matrix of 4,4'-diaminodiphenyl sulfone (DDS). Panels reproduced with permission
900 from: **c,d**, ref.⁵⁸ Wiley-VCH; **e-g** ref.⁶⁰, Springer Nature Ltd.

901

902

903

904

905 **Fig. 4 NIR emission from colloidal QDs.** **a**, Normalized photoluminescence from QDs with a core-
906 shell structure (shown as inset). **b**, QD-in-perovskite approach: radiative recombination dominates when
907 QDs and perovskite are lattice matched (left). Lattice mismatch causes interfacial defects (dash line)
908 and non-radiative recombination (right). **c**, Variation of EQE with J in devices using mixed halide
909 perovskite matrices with different iodine molar concentrations. **d**, The emitter only QD array approach:
910 The pink spheres are the emissive QDs and purple spheres represent defective QDs. The charge-
911 collection zones illustrated as yellow circles around the QDs are defined by the carrier diffusion length
912 (L_d). **e**, The matrix inclusion architecture: large QD are dispersed in a matrix of smaller QDs. Radiative
913 recombination channels (green circles) increase whereas non-radiative recombination channels decrease.
914 **f**, EQE of the single, binary and ternary devices plotted against injected current. Panels reproduced with

915 permission from: **a**, ref.⁷⁵, Springer Nature Ltd; **b,c**, ref.⁹⁹, Springer Nature Ltd; **d,e,f**, ref.¹⁰³, Springer
916 Nature Ltd.

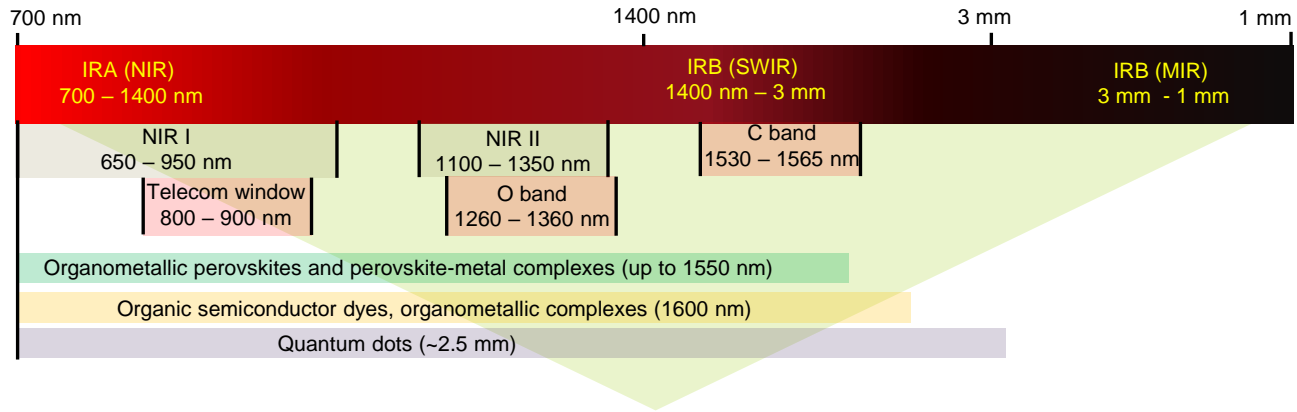
917



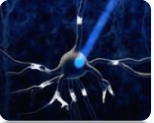
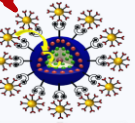

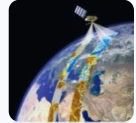

918

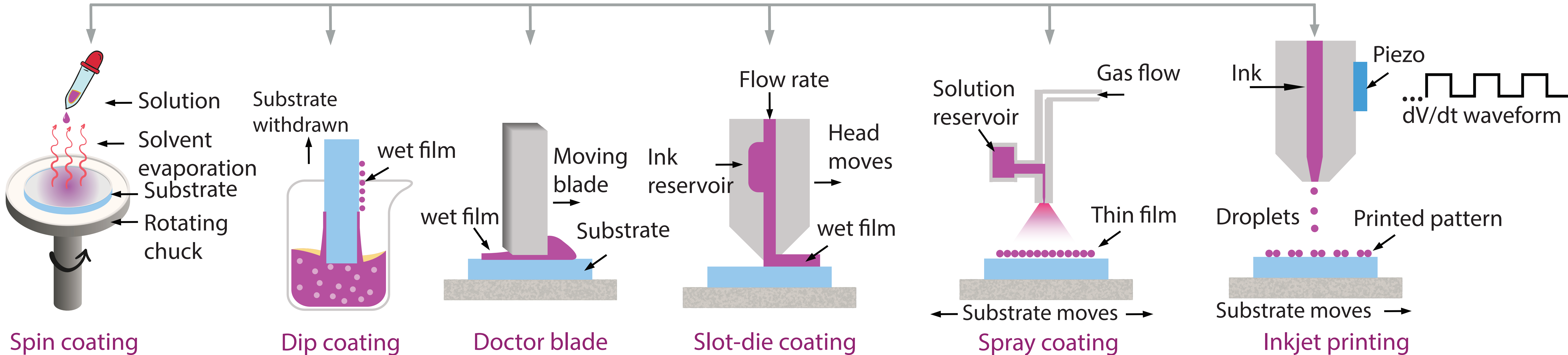
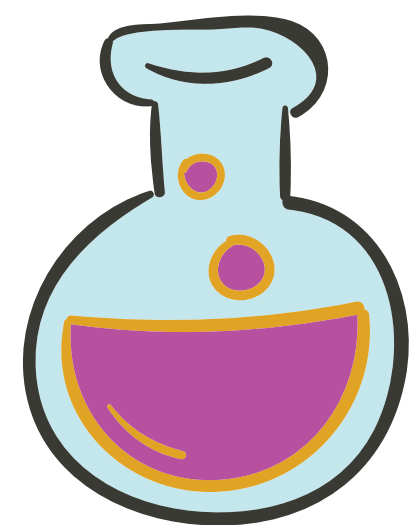
919

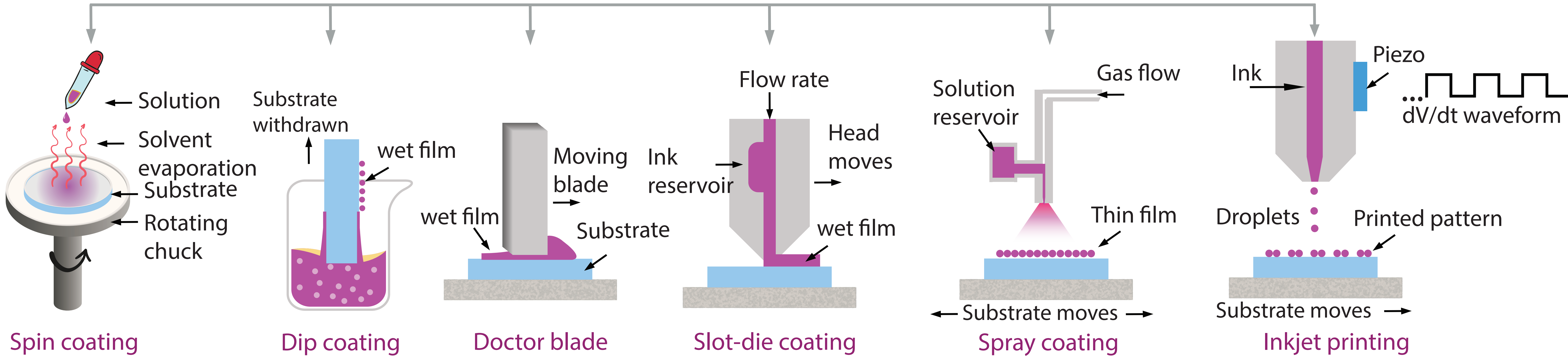
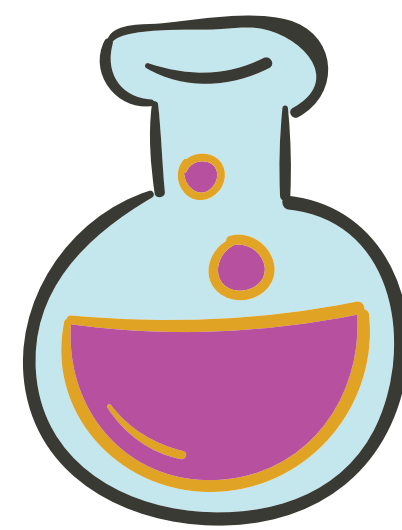
920 **Fig. 5 Figure of merits of NIR-LEDs.** **a**, EQE-wavelength of solution-processed NIR-LEDs based on
921 results of Supplementary Table 1. **b**, EQE roll-off of state-of-the-art TADF³² and phosphorescence⁴⁰
922 OLED, QDLED¹⁰³, hybrid (QD-in-perovskite) QDLED¹⁰¹, 3D⁶¹ and 2D⁶⁵ PeLEDs and 3D μ -PeLED¹²⁸
923 as a function of current density. **c,d**, Reported lifetime of various solution-processed NIR-LEDs based
924 on the data provided in Supplementary Table 2. In Fig. 5c the lifetime is plotted versus the initial device
925 radiance (given in $\text{W sr}^{-1} \text{m}^{-2}$) except for the OLED device where the initial irradiance is presented. In
926 Fig. 5d the lifetime is plotted versus injected current density into the device. T_{85} and T_{50} (or half-
927 lifetime) denote the time of constant operation until the light output decreases to 85% and 50%,
928 respectively, of the initial value.

929



Data storage	Imaging	Optogenetics	Biosensing	Optical communications	Remote sensing	Night vision
						





Spin coating

Dip coating

Doctor blade

Slot-die coating

Spray coating

Inkjet printing

